

# Open-access operating algorithms for commercial videokeratographer and improvement of corneal sampling

Julián Espinosa,<sup>1,2,\*</sup> David Mas,<sup>1,2</sup> Jorge Pérez,<sup>1,2</sup> and Ana Belén Roig<sup>2</sup>

<sup>1</sup>Instituto Universitario de Física Aplicada a las Ciencias y las Tecnologías (IUFACyT), Universidad de Alicante, Carretera San Vicente del Raspeig s/n, San Vicente del Raspeig, Alicante 03690, Spain

<sup>2</sup>Departamento de Óptica, Farmacología y Anatomía, Universidad de Alicante, Carretera San Vicente del Raspeig s/n, San Vicente del Raspeig, Alicante 03690, Spain

\*Corresponding author: julian.espinosa@ua.es

Received 25 September 2012; revised 19 November 2012; accepted 10 December 2012;  
posted 11 December 2012 (Doc. ID 176838); published 21 January 2013

We present an algorithm to process images of reflected Placido rings captured by a commercial videokeratoscope. Raw data are obtained with no Cartesian-to-polar-coordinate conversion, thus avoiding interpolation and associated numerical artifacts. The method provides a characteristic equation for the device and is able to process around 6 times more corneal data than the commercial software. Our proposal allows complete control over the whole process from the capture of corneal images until the computation of curvature radii. © 2013 Optical Society of America

OCIS codes: 330.7327, 100.2000.

## 1. Introduction

Commercial videokeratometers provide useful information about corneal topography and the tear film quality. Some of them are capable of continuous recording of the eye, a fact that allows the analysis of dynamic changes in the corneal surface [1,2]. However, none of available devices allows full control of the camera and processing algorithms. In all the cases, the information in obtaining a corneal topography is hidden, in spite of being of interest for researchers. Additionally, data maps are usually sparse, providing low data density, typically below 100 samples/mm<sup>2</sup>, and the surface map is often completed through numerical interpolation.

Among commercial Placido-based videokeratoscopes, the Medmont E300 (Medmont Pty., Ltd., Victoria, Australia) has shown to have a high degree of accuracy and precision for measuring spherical

and aspherical test surfaces [3] and high repeatability of measurements of *in vivo* corneas [4]. The device automatically captures four corneal topography images once the projection head, which includes the camera, is properly situated [5]. As a result, the system offers a clear image of the reflected Placido rings. Through the software package, it is possible to obtain the curvature maps and export the data to an ASCII file that can be later processed.

Even though main data can be exported, they have already been processed, and algorithms and system specifications are not available due to proprietary reasons. Therefore, results are not always reproducible by the user. Some works in the literature [6–8] try to improve videokeratography algorithms avoiding proprietary limitations. In [6], the authors detail the algorithms and procedures to recalibrate a topographer and obtain the raw data of corneal curvature. Briefly, the key point to the calculation of the curvature radius at a point consists of a correct detection and labeling (ordering) of the projected rings. The system is previously calibrated using a

set of spheres of known curvature radii. Then, the curvature radius data are obtained through linear interpolation.

An important drawback of these customized methods comes from the Cartesian-to-polar-coordinate conversion of the image, which is usually performed under the assumption of facilitating the image processing due to advantages from the symmetry of the rings. A correct conversion needs a precise knowledge of the center position. Since the cornea is not a symmetric spherical surface, contrary to what is assumed in the Cartesian-to-polar conversion, projected rings are neither completely circular nor concentric. This lack of circular symmetry of the rings leads to a loss and distortion of acquired information, while the fact that any ring has different center position may introduce prismatic effects and high-order aberrations that do not correspond to reality.

In order to overcome these problems, we present an algorithm to process captured images of reflected Placido rings. It avoids Cartesian-to-polar-coordinate conversion of corneal data and the subsequent interpolation. The proposal consists of building an interpolation surface with the help of calibration spheres of known radius. Placido rings reflected in the curved surface are segmented and classified through an elliptical scanning algorithm. Then, data are fitted to a unique calibration equation that characterizes the topographer. This equation and the scanning algorithm are finally used to process captured images of human corneas and get curvature radii.

The manuscript is structured as follows: the method is presented in Section 2. In Section 3, we check the reliability of the algorithm by measuring the set of steel spheres. The method is also applied to a human cornea, and the result is compared with data provided by a Medmont topographer. Finally, the main outcomes of the proposal are underlined in the Conclusions Section.

## 2. Method

The experimental setup was adapted from the one described in [6]. Polished metal spheres of known radius were measured with a Medmont E-300 corneal topographer. At this point, the use of one or another

device is irrelevant. The main advantages of the E-300 are the possibility of removing the color map and accessing to the original image of the reflected rings. The device is manually focused, so skilled operators are recommended to take measurements. The captured images were then processed with MATLAB following procedures designed by the authors. As we stated in Section 1, the main new features of the method are related to the software, which has been redesigned to overcome the previously exposed drawbacks.

### A. Ring Extraction: Frame Binarization

The camera of the topographer provides a gray-scale image of the reflected rings [Fig. 1(a)]. First, we need to identify and isolate each ring. Unfortunately, gray level varies much across the image, so the image contrast needs to be optimized prior to further manipulation. In order to enhance the contrast, we use the morphological operators opening and closing top-hat filters.

Gray-scale morphology is a powerful tool to analyze and process geometrical structures inside images. The most basic operations of gray-scale morphology are erosion  $\ominus$  and dilation  $\oplus$ , whose definitions can be found elsewhere [7]. The opening and closing operation of an input image  $F$  by a structuring element  $B$  are defined by

$$F \circ B = (F \ominus B) \oplus B, \quad (1a)$$

$$F \cdot B = (F \oplus B) \ominus B, \quad (1b)$$

respectively. The opening and closing top-hat operations are defined from them as

$$\text{OTH}_{FB} = (F - F \circ B), \quad (2a)$$

$$\text{CTH}_{FB} = (F \cdot B - F). \quad (2b)$$

Top-hat operation has some characteristics of high-pass filtering. The opening and closing top-hat operations can detect wave crests or hollows in an image, respectively. Therefore, from the initial image [Fig. 1(a)], we perform, on the one hand, an opening top-hat operation with a disk-shaped flat

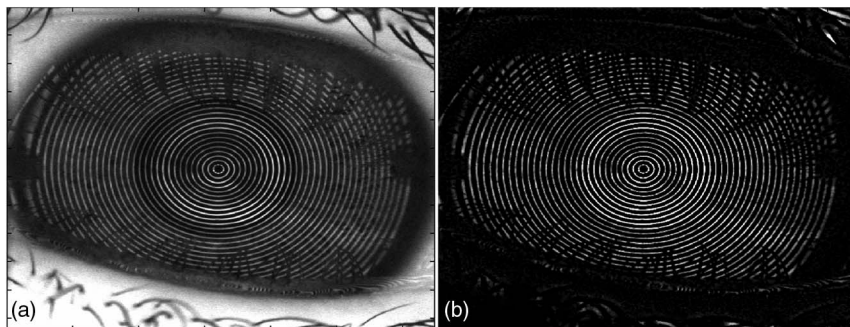


Fig. 1. (a) Initial frame. (b) Open minus close top-hat filtered frame.

structuring element of radius 5 pixels. On the other hand, using the same structuring element, we operate a closing top-hat operation also over the initial frame. Then contrast is improved by subtracting the closed top-hat from the open top-hat filtered images, as can be seen in Fig. 1(b).

The filtered frame is then binarized, recentered, and cropped or zero padded to a square matrix [Fig. 2(a)]. The next task consists of identification and correct classification of Placido rings.

#### B. Ring Labeling: Elliptical Scanning Algorithm

The elliptical scanning algorithm is an effective method to individually detect and label the projected rings. It defines an elliptical annulus one pixel wide, which grows pixel per pixel and scans the image from center to periphery. The scanning is used to detect and label each ring.

First, the center of the topography is estimated by calculating the centroid in the clean image. Then the amount and radii of the rings is estimated just by counting the lines through the longest meridian. Usually, it is from the center to nose, mainly because the shadows of the eyelashes block other directions.

From the center of the figure, the scanning starts with an annulus of radius one, or at least lower than the location assigned to first ring in the meridian. The annulus grows pixel by pixel until a pixel different to zero is detected. The detected ring is labeled according to its ordered position from the center. The annulus continues growing and adding pixels to this ring until it again detects all pixels equal to zero, i.e., when the scanning annulus reaches the gap between two consecutive rings.

Pixels that form a ring are fitted to an ellipse, thus obtaining its geometrical parameters (center coordinates, size of the axes, and tilt). These parameters are used to implement the elliptical annulus that will continue the scan. The process is repeated until the algorithm is unable to discern a unique ring. In Fig. 2(b), we present a frame of the elliptical scanning (Media 1). It correctly detects up to 29 rings that correspond approximately to the whole iris.

The typical approach establishes that, from each classified ring, one can obtain two edges just by isolating the inner and outer perimeter pixels. This way, the density of the radial sampling is increased. Nevertheless, in real eyes, eyelashes and other reflections cause broken rings that difficult a direct ring-to-edge conversion. In order to avoid errors, the double-edge extraction is only done when possible, i.e., when the ring is not broken (Fig. 3). This usually happens in the pupil area, which is the most important to determine the image quality. In the shown case, we go from 29 labeled rings [Fig. 2(b)] to 39 different radial distances.

#### C. Image Calibration

In order to have a full control over the calculation of the corneal maps, we propose our own calibration algorithm. Thus, from the labeled rings, a point-to-point curvature map of the cornea will be calculated. Some authors describe this method as the look-up table or calibrated-spheres algorithm [8–10]. In [6], the authors used 18 steel spheres of known curvature radius with an accuracy of 10  $\mu\text{m}$  to obtain a set of calibration curves that describe each of the reflected rings. The curvature radius of the calibration surface  $\rho$  for each labeled ring  $l$  was related to the mean radial distance  $R$ , i.e., the ring radius, through

$$R = m_l \rho + n_l, \quad (3)$$

where  $l = 1, \dots, L$  represents the ring labels, and  $L$  is the maximum number of detected rings. Mean radial distance was computed as the average of the distances obtained after transforming the image from Cartesian to polar coordinates. Unfortunately, as we pointed above, this approach may introduce important calibration errors.

In this work, we used 12 spheres of curvature radii ranging from 7 to 10 mm, and we apply the elliptical scanning ring algorithm in order to detect, join, and label the pixels belonging to each ring. We propose obtaining a calibration surface, i.e., a unique calibration equation that depends on  $\rho$  and  $l$  alternatively to the set of calibration curves in Eq. (3).

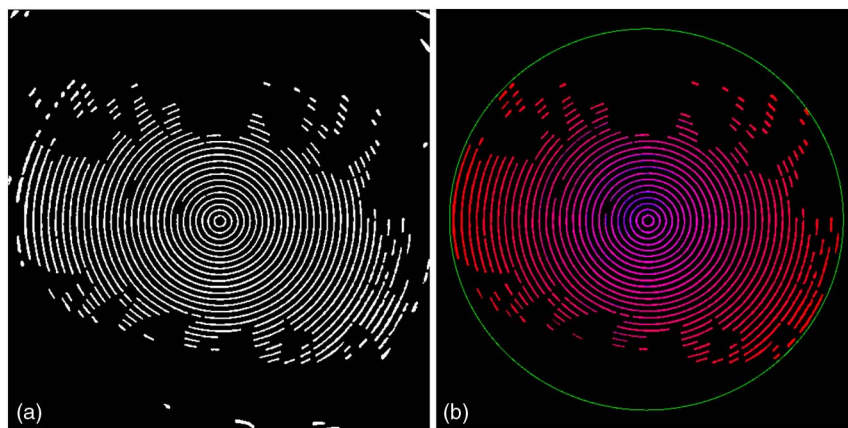


Fig. 2. (Color online) (a) Initial binarized frame. (b) Final-frame excerpts from video of the labeling of projected rings through the scanning annulus (Media 1).

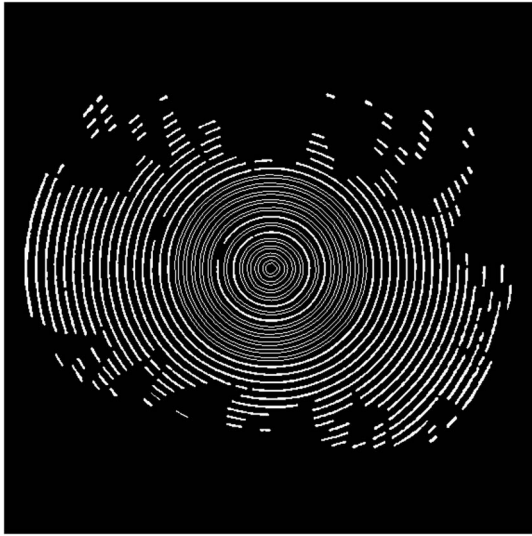


Fig. 3. Detected rings and edges obtained from the inner and outer perimeters of those which are not broken.

### 3. Results

Following the above-described algorithms from the known curvature radii and by classifying reflected rings, we just need to estimate the mean radial distance. Now,  $R$  is set as the radius obtained from fitting a circumference to each ring. We have fitted data from calibration spheres to Eq. (3) and represented both  $m_l$  and  $n_l$  as a function of  $l$  in Fig. 4. Both parameters show a linear dependence on the label, which can be expressed as  $m_l = pl$  and  $n_l = ql$ . Hence, if we come back to Eq. (3) and introduce a linear dependence on  $l$ , we get the calibration formula

$$R = pl\rho + ql \rightarrow R = pl\left(\rho + \frac{q}{p}\right) \rightarrow R = pl(\rho + s), \quad (4)$$

which only stands for the curvature operation range of the topographer. Now, coefficients  $p$  and  $s$  are obtained through least-squares fitting the calibration

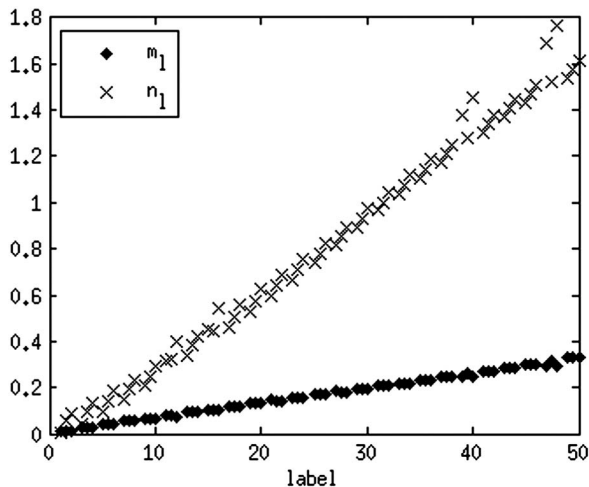


Fig. 4. Slopes and ordinates at origin as a function of the labels.

parameters to Eq. (4), i.e., the sphere curvature radii and radial distances of reflected rings. Following Eq. (5), we can obtain the curvature radius  $\rho(x,y)$  at any point  $(x,y)$  of a ring reflected on an unknown curved surface. We just have to determine the label  $l_{(x,y)}$  and the distance  $R(x,y)$  from this point to the center of the frame:

$$\rho(x,y) = \frac{R(x,y)}{pl_{(x,y)}} - s, \quad (5a)$$

$$\Delta\rho(x,y) = \frac{R(x,y)}{p^2l_{(x,y)}}\Delta p + \Delta s. \quad (5b)$$

$\Delta\rho(x,y)$  is the absolute error in the radius determination. Notice that we provide a unique calibration equation, alternatively to the set of curves in [6].

Furthermore, the consideration of both rings and edges increases the accuracy in the measurement of the surface since it results in a denser sampling. However, it also implies obtaining two different calibration surfaces. It depends on whether we consider the rings or the edges. In order to avoid this, both edges and rings can be consecutively labeled from center to periphery. Edges are classified with integer numbers, whereas for rings, we take into account that they match the gap between two consecutive edges, so they are labeled with the corresponding integer and a half.

Hence, we have processed images from the calibration spheres and least-squares fitted to Eq. (4) the data for edges, rings, and both them (596, 346, and 942 points, respectively). Obtained parameters are shown in Table 1.

All the fittings provide similar parameters, low root-mean-square errors (RMSEs), and a high correlation between variables. In Fig. 5, we present the calibration surface obtained if we only consider the rings.

We have checked the consistency of the method just by applying the algorithm to measure the curvature radius of each sphere used in the calibration process. Our algorithm provides between 45,000 and 59,000 raw curvature points (it depends on the sphere) sampled in a  $580 \times 580$  matrix. It implies a sampling average of  $420 \text{ mm}^{-2}$ , which is 4 times better than resolutions obtained in typical commercial devices.

We have averaged out the obtained curvature radii and have compared them with the real ones (Fig. 6). The errors in the mean curvature radii are around 0.07 mm. If we suppose a spherical cornea of radii 8 mm, that mean error implies a 0.25 diopter indetermination in the corneal power, which is in the limit of clinically detectable error. In Fig. 6, we also compare the averages of data provided by Medmont and the real ones. Both serial data have been fitted to the equation  $C_{\text{mean}} = aC_{\text{real}}$  showing a good agreement, as one can see in Table 2.



Table 1. Parameters of the Calibration Surface Obtained from the Fitting to Eq. (4)

	$p(\times 10^{-3})$	$\Delta p(\times 10^{-3})$	$s$ (mm)	$\Delta s$ (mm)	RMSE (mm)	$R^2$
Edges	9.27	0.03	2.34	0.03	0.02	0.999
Rings	9.31	0.03	2.30	0.04	0.02	0.999
Edges and rings	9.28	0.02	2.32	0.03	0.02	0.999

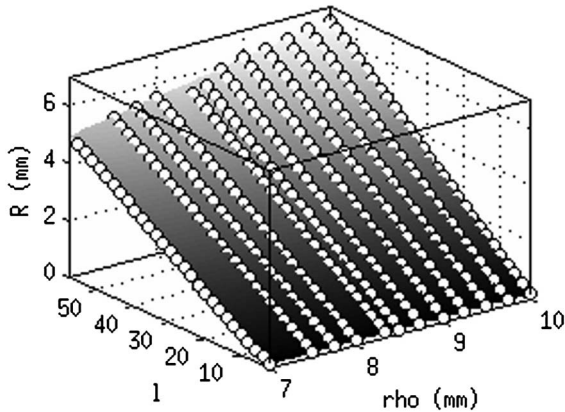


Fig. 5. Calibration surface obtained just taking into account the rings.

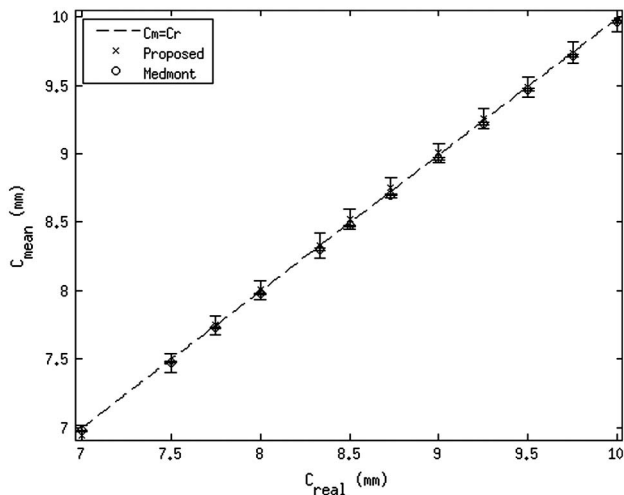


Fig. 6. Mean curvature radii of the calibration spheres obtained both by our algorithm and Medmont.

In order to clarify the differences between both approaches, in Fig. 7 we show the sampling distribution obtained following the different methods discussed here. We represent our obtained samples (raw data) versus radial distance, compared with a standard

Table 2. Parameter Coefficients for the Fitting Used to Check the Consistency of the Method

	$a(\text{mm}^{-1})$	$\Delta a(\text{mm}^{-1})$	RMSE (mm)	$R^2$
Proposal	0.9990	$8e-4$	$6e-3$	0.999
Medmont	0.99660	$1e-5$	$1e-4$	1

Cartesian sampling of  $100 \text{ mm}^{-2}$  and with constant radial sampling density provided by Medmont, in a Cartesian quadrant for a real eye. Note that samples in the standard case fall at high radial distance due to the lack of data (eyelash shadows). At this point, we would like to underline that the E300 software provides the facility to export topographic data for the selected exam to a set of text files. Those data are axial and tangential curvatures, surface height, radial distance, and surface slope data. Each line of the files contains the data of a single meridian (centered at the keratometric axes) with data points for each ring. There are 300 meridians each with 32 samples, i.e., the number of rings. However, this uniform radial sampling does not match the data captured with a CCD, so we guess that these are processed data. Contrary to our case, data provided are not raw data but computed through proprietary algorithms.

In order to make clear the differences between both approaches, we have compared results of a real corneal measurement. Curvature data usually provided by Medmont are shown in Fig. 8(a). There are around 5000 sampled points with a spatial frequency of  $64 \text{ mm}^{-2}$ . In Fig. 8(b), we represent data obtained through our method. There are 30,113 sampled points with a spatial frequency of  $360 \text{ mm}^{-2}$ . Therefore, in this case, our method allows us to analyze around 6 times more data than those provided by Medmont.

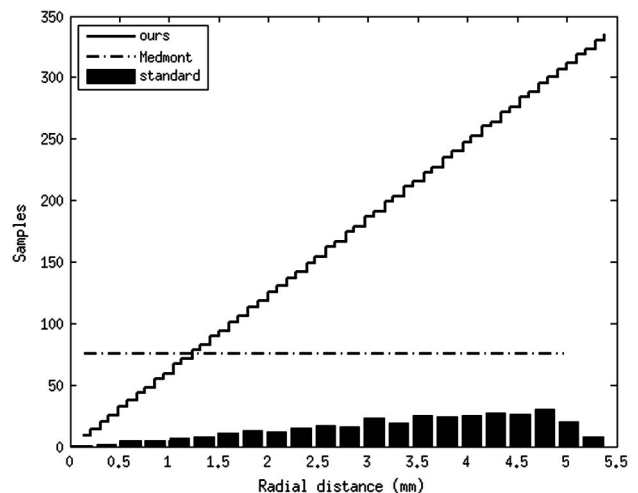


Fig. 7. Real samples using the posed method versus radial distance compared with those for a standard Cartesian sampling of  $100 \text{ mm}^{-2}$  and with constant radial sampling density provided by Medmont, in a Cartesian quadrant obtained for a real eye.

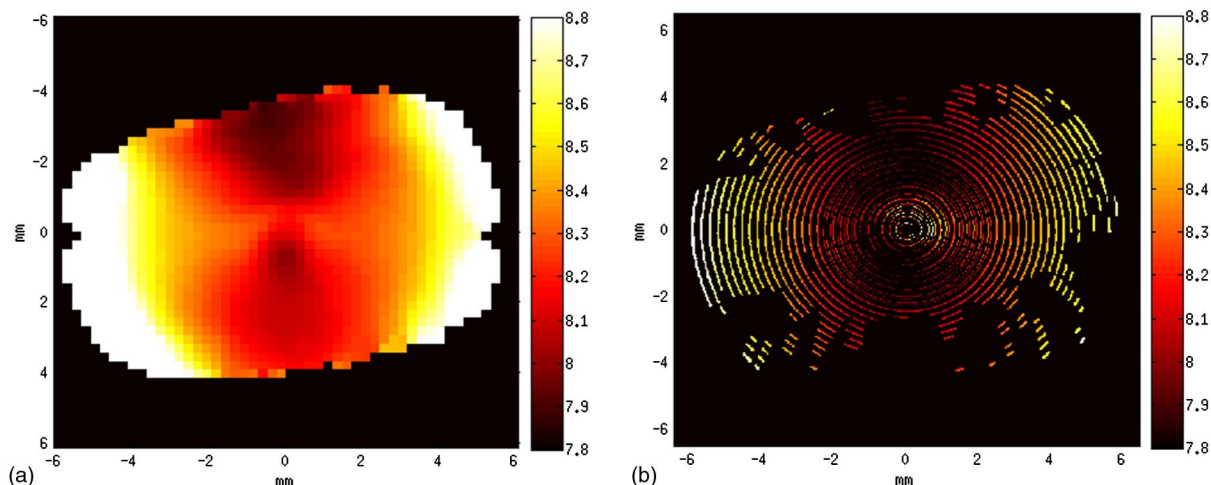


Fig. 8. (Color online) (a) Curvature radii from Medmont. (b) Obtained curvature radii.

#### 4. Conclusion

Open access to the software and to the parameters of the video camera permits more complex experiments than those that can be done with a commercial device. Thus, with the help of the E300 videokeratoscope platform, we have built an equation to characterize the curvature radius computation. The method can be easily adapted to work on any topographer so that it can provide additional information about the cornea at no additional cost.

In [11], the authors propose applying weighted least-squares regression that compensates the unequal influence of sectors due to the sampling distribution. They argue that traditional least-squares fitting on an optical surface does not pay attention to the particular sampling distribution of the analyzed surfaces. The adequate distribution of the samples depends both upon the geometry of the domain and the properties of the approximating functions. The uniform  $(x, y)$  grid is better suited for translational-invariant domains and functions and not for rotationally symmetric polynomials on a disk. However, the conversion from a uniform Cartesian grid to a polar one provides both radial and angular sampling not uniformly spaced.

The elliptical scanning algorithm allows an analysis of annular regions of the surface. This fact reduces the unequal density of samples in different sectors of the sampled surface and allows the improvement of optical surfaces fitting. Therefore, despite the method not completely overcoming the above exposed sampling inconvenience, it avoids the angular sampling interpolation.

From the algorithms here presented, it is possible to introduce convenient modification in the calibration process and temporal and spatial resolution of the camera and the numerical algorithms to obtain new information about dynamic processes in the cornea and the tear film. The method provides a higher density of corneal curvature data, which makes possible the analysis of small corneal defects, evolution of scars, ulcers, etc. Additionally, it avoids

proprietary rights and patents, so all the measuring process is controlled.

The authors provide the computation algorithms upon request. The authors would like to acknowledge the financial support of the Spanish Ministerio de Ciencia e Innovación through the project BIA2011-22704, the Generalitat Valenciana through the project PROMETEO/2011/021, and the University of Alicante through the project GRE10-09. A. B. Roig thanks Fundación Cajamurcia for the grant “Beca de investigación Cajamurcia 2010.”

#### References

1. T. Goto, X. Zheng, S. D. Klyce, H. Kataoka, T. Uno, M. Karon, Y. Tatematsu, T. Bessyo, K. Tsubota, and Y. Ohashi, “A new method for tear film stability analysis using videokeratography,” *Am. J. Ophthalmol.* **135**, 607–612 (2003).
2. D. R. Iskander and M. J. Collins, “Applications of high-speed videokeratoscopy,” *Clin. Exp. Optom.* **88**, 399–407 (2004).
3. W. Tang, M. J. Collins, L. Carney, and B. Davis, “The accuracy and precision performance of four videokeratoscopes in measuring test surfaces,” *Optom. Vis. Sci.* **77**, 483–491 (2000).
4. P. Cho, A. K. C. Lam, J. Mountford, and L. Ng, “The performance of four different corneal topographers on normal human corneas and its impact on orthokeratology lens fitting,” *Optom. Vis. Sci.* **79**, 175–183 (2002).
5. S. A. Read, M. J. Collins, L. G. Carney, and R. J. Franklin, “The topography of the central and peripheral cornea,” *Invest. Ophthalmol. Visual Sci.* **47**, 1404–1415 (2006).
6. D. Mas, M. A. Kowalska, J. Espinosa, and H. Kasprzak, “Custom design dynamic videokeratometer,” *J. Mod. Opt.* **57**, 94–102 (2010).
7. J. Serra, *Image Analysis and Mathematical Morphology* (Academic, 1983).
8. L. A. V. De Carvalho, A. C. Romao, S. Tonissi, F. Yasuoka, J. C. Castro, P. Schor, and W. Chamon, “Videokeratograph (VKS) for monitoring corneal curvature during surgery,” *Arq. Bras. Oftalmol.* **65**, 37–41 (2002).
9. C. Roberts, “Characterization of the inherent error in a spherically-biased corneal topography system in mapping a radially aspheric surface,” *J. Refract. Corneal Surg.* **10**, 103–111 (1994).
10. S. A. Klein, “Corneal topography: a review, new ANSI standards and problems to solve,” in *Vision Science and its Applications*, OSA Technical Digest (Optical Society of America, 2000), paper NW8.
11. J. Espinosa, J. Pérez, D. Mas, and C. Illueca, “Weighted Zernike polynomial fitting in steep corneas sampled in Cartesian grid,” *J. Mod. Opt.* **58**, 1710–1715 (2011).